

Risk-aware Distributed Coordination of Peer-to-peer Energy Trading for Electric Vehicle Charging Stations in Constrained Hierarchical Power Distribution and Urban Transportation Networks under Uncertainties

Xianlong Chen, Xiuli Wang, *Senior Member, IEEE*, Mohammad Shahidehpour, *Life Fellow, IEEE*

APPENDIX A: TEST CASE DESCRIPTION AND SYSTEM DATA

To verify the effectiveness of the proposed coordination framework and model, several EVCSs with distributed PV or BESS in constrained PDN and UTN are investigated. In this paper, the 12-node UTN and the modified IEEE 33-bus three-phase PDN are used for our studies as displayed in Fig. A1. The parameters of UTN and PDN are provided in [G1],[G2] (See Appendix G). The origin-destination (O-D) pairs and the corresponding traffic demand forecast value of UTN are from [G2] as listed in Table A.I, where the standard deviation of traffic demand forecast error is set as 5% of the expected value. The time cost coefficients of free and delay travel are set as 0.2\$/min and 0.4\$/min, respectively. The individual EV capacity is generated from 40kWh to 64kWh, randomly. The installed PV capacities of EVCSs are range from 200kW to 250kW, and the installed local BESS capacities are range from 150kWh to 250kWh. The energy procurement price from PDN is displayed in Fig. A2, and the energy sale price to PDN is fixed as 0.014\$/kWh. The Spearman correlation coefficients between renewables and electric load are revised from [G3] and [G4].

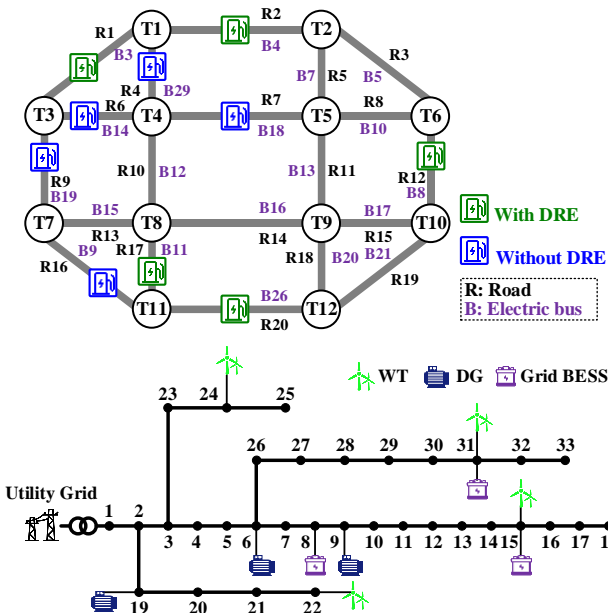


Fig. A1. UTN and PDN topology and their correlations

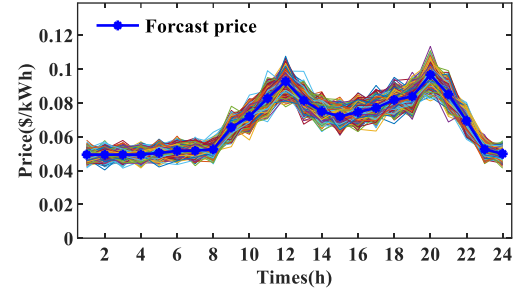


Fig. A2. Forecast PDN electricity price and its uncertain scenarios

TABLE A.I

O-D PAIRS AND TRAFFIC DEMAND IN UTN						
O-D pairs	1-12	2-7	3-11	6-3	7-6	10-1
Traffic demand	600	800	500	500	800	600

TABLE A.II
THE PARAMETERS OF DGs

DG	Bus	$P_{dg,min}^{dg} / P_{dg,max}^{dg}$	RU	RD	$\theta_{min}^{dg} / \theta_{max}^{dg}$	b_2	b_1
1	6	0/0.86	0.52	0.52		9×10^{-3}	58
2	9	0/0.76	0.38	0.38	0/0.9	10×10^{-3}	60
3	19	0/0.98	0.72	0.72		11×10^{-3}	62

$P_{dg,max}^{dg}, P_{dg,min}^{dg}$: maximum/minimum power output (MW)

RU, RD : maximum up/down ramp rate (MW/h)

$\theta_{max}^{dg}, \theta_{min}^{dg}$: maximum/minimum power factor

Generation cost: $b_2 P^2 + b_1 P$ (\$), where b_2 (\$/MW²), b_1 (\$/MW)

TABLE A.III
THE PARAMETERS OF GRID BESSs

BESS	Bus	E^{max}	E^{min}	$P^{ch,max}$	$P^{dis,max}$	η^{ch} / η^{dis}
1	8	0.46	0.046	0.17	0.17	
2	15	0.52	0.052	0.18	0.18	0.9
3	31	0.42	0.042	0.16	0.16	

$P^{ch,max}, P^{dis,max}$: maximum charging/discharging power (MW)

E^{max}, E^{min} : maximum/minimum energy storage (MWh)

η^{ch}, η^{dis} : Charging/discharging efficiency

Degradation cost: $c_0(P^{ch}\eta^{ch} + \frac{P^{dis}}{\eta^{dis}})$

In addition, the PDN contains three DGs, three grid BESSs and four WTs, which locations are also displayed in Fig. A1. The detailed parameters of DGs and grid BESSs are listed in Table A.II and Table A.III, and the rated power of each WT is 160 kW. The degradation costs of grid BESSs are provided in [G2]. The WT and load forecast data are offered in [G5] and [G2], respectively. The energy purchase price from upstream

grid (UG) for DSO is the same as the PDN electricity price, which value is displayed by the blue line in Fig. A2. The price for the reactive power purchased from external ancillary service market and local flexible recourse are set as 20% of the UG electricity price. The reserve prices of local flexible recourses are from [G6]. The secure voltage range is from 0.9 p.u. to 1.1 p.u.. The maximum VUR is set as 3%, which can be adjusted according to different operation requirements by DSO.

APPENDIX B: ADDITIONAL RESULTS

B1. Charging load simulation results

The expected EV charging load and various charging scenarios are obtained after the EV charging load simulation using MCM in constrained UTN. Fig. B1 displays the expected hourly EV charging load assigned to individual EVCSs from UTN. Here, only eight EVCSs 3, 4, 8, 9, 11, 19, 26 and 29 procure EV charging load from UTN in the scheduling period. The EV charging demands of EVCSs are mainly concentrated in 7th-21th timeslots, and EVCS 4, 11, 19 and 26, take up most of the charging load, i.e., up to 70.6% of the total EV charging load, in the scheduling period. The detailed EV charging load simulation of EVCS 8 and 19 are listed in Fig. B2 including the expected value and various charging scenarios. After the simulation, the expected EV charging load and various charging scenarios are sent to EVCSs for energy scheduling and uncertainty set construction.

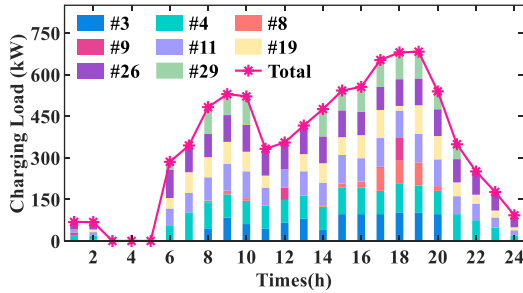


Fig. B1. Expected charging load assigned to individual EVCSs from UTN

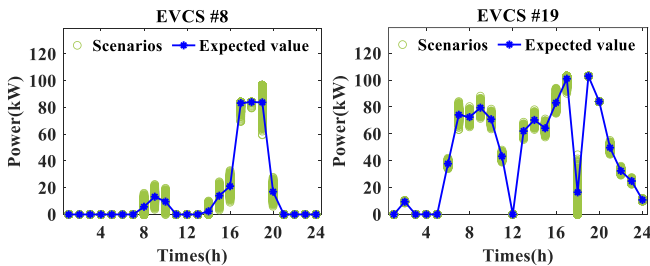


Fig. B2. Detailed EV charging load simulation of EVCS 8 and 19

B2. Performances of P2P-TE scheme and DRO technique

1) *Effectiveness of P2P-TE trading*: Table B.I summarizes the energy exchange profiles and total operation cost of EVCSs with and without P2P-TE trading. As shown, the total EVCS operation cost is reduced from \$262.11 to \$192.25, i.e., a 26.65% drop after implementing the P2P-TE trading. The P2P-TE trading among EVCSs can reduce the dependence on the expensive electricity from PDN as energy sales to PDN continue to decline. In essence, the expensive energy purchase from PDN is declined by nearly 28.54% from 4423kWh to 3160.6kWh.

2) *Performance of the DRO scheme in P2P-TE trading*: In this subsection we compare the performance of our proposed DRO-based model with another two benchmark approaches, i.e., stochastic programming scheme, denoted as SP, and robust optimization scheme, denoted as RO. The SP problem is constructed based on multi-scenarios method [15], and the RO problem searches for the optimal value under the worst situation of uncertainties [17]. Fig. B3 illustrates the optimal value of the overall operation cost using SP, RO and DRO schemes with different sample sizes, where the confidence level of chance constraint (7j) in the DRO scheme is set as 95%. As observed, the RO scheme brings the highest operation cost due to the excessive conservativeness, while the SP scheme yields the lowest operation cost owing to its optimism. The operation cost of the DRO scheme is between those of RO and SP since it denotes the minimum operation cost under the worst-case distribution in the ambiguity set. Therefore, the DRO advantage for balancing the conservatism and optimism is validated.

Note that the operation cost of the DRO scheme decreases with the increase in sample size since the ambiguity shrinks with more historical data included. Fig. B4 depicts the total operation cost under various confidence levels of chance constraint (7j), where the sample size is 1000. The total operation cost grows with the increase in confidence level since more energy procurement is required to satisfy the random electric demand at a higher confidence level.

	TABLE B.I COMPARISON WITH/WITHOUT P2P-TE TRADING		
	Without P2P-TE trading	With P2P-TE trading	Variation (%)
Power from PDN (kWh)	4423	3160.6	↓ 28.54%
Power to PDN (kWh)	3083.6	1805.8	↓ 41.44%
Power from/to peers (kWh)	-	1418.9	-
Total operation cost (\$)	262.11	192.25	↓ 26.65%

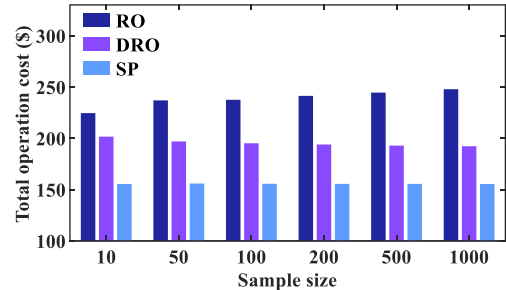


Fig. B3. Comparison of total operation cost using schemes with different sample size

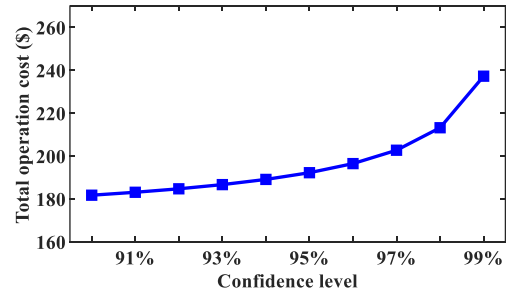


Fig. B4. Comparison of total operation cost for various confidence levels

3) *Merits of the DR-CC method on DSO operation*: Table B.II displays the total operation cost of the day-ahead dispatch for SP-based stochastic case, RO-based robust case, and DR-CC case. From Table B.II, the SP case has the lowest operation cost

due to their persistently optimism and the RO case has the largest cost due to the excessive conservatism, while the proposed DR-CC approach which can overcome the shortcomings and make a good compromise between operation security and economic efficiency has the intermediate cost.

TABLE B.II
TOTAL OPERATION COST USING DIFFERENT METHODS

Method	SP Case	RO Case	DR-CC Case
Total Cost (\$)	2575.2	3211.8	2659.7

The after-the-fact situations are analyzed here to further illustrate the merits of the proposed DR-CC method. The following three schemes are discussed to compare the operation costs and PDN security operation performances under the worst after-the-fact situations, which means the worst uncertainty realizations of minimum renewable generation and maximum electric load.

- ♦ *Scheme I* (SP case): The day-ahead PDN electricity scheduling is determined by the multi-scenario SP method [22], where all uncertain deviations of renewable and electric load are balanced by UG.
- ♦ *Scheme II* (Linear robust case without the correlation of uncertainties): A chance-constrained linear robust method [18] is adopted to determine the energy & reserve scheduling. The uncertain deviations are balanced by local flexible resources and UG, without considering the correlation among uncertainties.
- ♦ *Scheme III* (DR-CC case considering the correlation among uncertainties): The energy and reserve scheduling are co-optimized by the proposed DR-CC method in this paper. The uncertain deviations are balanced by local flexible resources, and the correlation among uncertainties is considered based on Spearman correlation characterization and multivariate Gaussian copulas.

Table B.III displays the operation costs of the worst after-the-fact situations using different schemes, where all the cost terms consist of day-ahead energy & reserve procurement costs and real-time balancing expenses. As shown, the active/ reactive power costs of UG in Scheme I are much higher than those of the other two schemes. Likewise, Scheme I has the largest after-the-fact operation cost as all the uncertainties are balanced by the relatively expensive UG supply. Compared to Schemes I and II, Scheme III can greatly reduce the after-the-fact operation cost by nearly 17.55% and 8.37%, respectively. In addition, the DER cost in Scheme III is the largest since the flexible reserve providers need to supply extra energy to balance the deviations.

In addition, compared to Schemes I and II, scheme III can enhance the operation performance of three-phase PDN in the worst after-the-fact situation as shown in Table B.IV. As shown, in scheme I, the voltage magnitude of each phase at each node ranges from 0.94087 - 1.0053 p.u., where the maximum VUR is up to 2.101%. However, this additional increase might not be approved in DSO's strict operation. For scheme II, the minimum voltage magnitude is under 0.95 p.u., despite the fact that the maximum VUR is under 2%, which might not be approved in a strict DSO operation.

Scheme III proposed in this paper can guarantee the best performance even in the worst after-the-fact situation. The maximum VUR of scheme III is the lowest compared with

Schemes I and II, and the minimum voltage magnitude is 0.95312. The detailed three-phase nodal voltage magnitudes of the worst after-the-fact situations using Schemes I, II and III at hour 8 are depicted in Fig. B5, where Scheme III has the best operation performance.

In summary, the proposed DR-CC scheme has the intermediate operation cost in the day-ahead scheduling, which strikes a balance between conservatism and optimism for managing uncertainties. In addition, compared to other schemes, the proposed DR-CC scheme can significantly reduce the after-the-fact operation costs and improve the operation performance when considering the uncertainty realization.

TABLE B.III
OPERATION COST IN THE AFTER-THE-FACT SITUATION (\$)

Scheme	Total cost	Active power cost of UG	Reactive power cost of UG	DER cost	Reserve cost
I	3320.91	1314.39	269.46	1737.06	-
II	2988.31	955.71	244.65	1756.96	30.99
III	2738.17	613.2	172.54	1868.26	84.17

TABLE B.IV
COMPARISON OF THREE-PHASE PDN OPERATION PERFORMANCES

Scheme	Maximum voltage amplitude (p.u.)	Minimum voltage amplitude (p.u.)	Maximum VUR (%)
I	1.0053	0.94087	2.101%
II	1.0052	0.94639	1.893%
III	1.0095	0.95312	1.855%

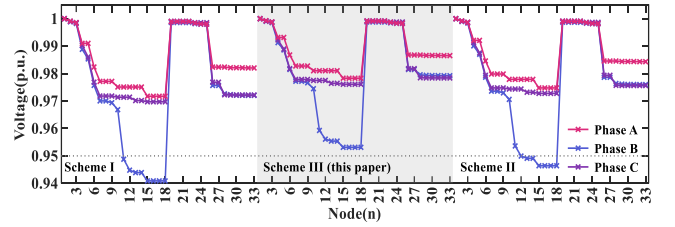


Fig. B5. Voltage magnitudes of the worst after-the-fact situations at hour 8

B3. Impact of Trading Adjustment Signal

The P2P-TE trading results among EVCSs are submitted to the DSO's TU-P-OPF model for feasibility evaluation. Here, we investigate the trading adjustment signal from the DSO to individual EVCSs when DSO constraints are violated. To illustrate the effect of trading adjustment signal, we implement a case that a 500kW PV is added in EVCS 18 on road R7 and the maximum permissible power flow on line 17, which is extended from node 18 to node 17, is limited to 300kW. This case could simulate the situation when the line under maintenance has a capacity that is below its designed capacity.

We solve the proposed TU-P-OPF model in (23) to find that line 17 will be congested in this case, and the PDN power flow will not be feasible without a P2P-TE trading adjustment among EVCSs. According to the solution of (23), there will be a power injection adjustment of -49.82 kWh at node 18, and DSO would send a trading adjustment signal of 300 kWh to EVCS 18 using (26) and (27). After receiving the trading adjustment signal, the EVCSs would adjust their energy scheduling & trading again, and resubmit the trading results to DSO. The follow-up TU-P-OPF results indicate that the DSO operation is feasible and the updated P2P-TE trading results can be executed through PDN after the trading adjustment.

APPENDIX C: DETAILED EV CHARGING LOAD ASSIGNMENT MODEL

The EV charging load assignment is implemented by TSO through solving the traffic flow assignment problem (TAP), which is formulated based on Nesterov model using primal-dual method [G1]. The EV charging expense is accommodated in the objective function through introducing the time-price factor for monetizing the travel time cost. Thus, the objective function of EV charging load assignment problem is to minimize the total travel and charging costs as follow:

$$\min F_{UTN}^{TSO} = F_{UTN}^{free}(\mathbf{x}^{ch}, \mathbf{x}^{non}) + F_{UTN}^{jam}(\mathbf{x}^{ch}, \mathbf{x}^{non}) + F_{EV}^{ch}(\mathbf{P}^{EV}) \quad (C1)$$

$$F_{UTN}^{free} = \sum_t \sum_a \lambda_a^{free} t_a^0 (x_{a,t}^{ch} + x_{a,t}^{non}), \forall a \in T_A^{free} \quad (C2)$$

$$F_{UTN}^{jam} = \sum_t \sum_a \lambda_a^{jam} (t_a^0 + t_{a,t}^{del})(x_{a,t}^{ch} + x_{a,t}^{non}), \forall a \in T_A^{jam} \quad (C3)$$

$$F_{EV}^{ch} = \sum_{t \in T} \sum_{h \in \Omega} \lambda_{h,t}^{ch} P_{h,t}^{ev} \quad (C4)$$

where $\mathbf{x}^{ch} = \{x_{a,t}^{ch}, \forall a, \forall t\}$ and $\mathbf{x}^{non} = \{x_{a,t}^{non}, \forall a, \forall t\}$ means the traffic flow vectors of charging and non-charging vehicles. $\mathbf{P}^{EV} = \{P_{h,t}^{ev}, \forall h, \forall t\}$ is the assigned charging power vector at EVCSs. The objective function (C1) contains three terms as expressed in (C2) - (C4), which are travel time cost on non-congested roads, travel time cost on congested roads and EV charging expense, respectively. λ_a^{free} and λ_a^{jam} indicates the time-price factors of non-congestion and congestion. t_a^0 is the free travel time of road a . $t_{a,t}^{del}$ is equal to the dual variable of (C6), which is regarded as the traffic delay time when occurring the road congestion. $\lambda_{h,t}^{ch}$ is the charging price of EVCS h . The UTN operation constraints are listed as follow:

$$x_{a,t} = x_{a,t}^{ch} + x_{a,t}^{non}, \forall a, \forall t \quad (C5)$$

$$x_{a,t} \leq c_a : \lambda_{a,t}, \forall a, \forall t \quad (C6)$$

$$\sum_{k \in K_{rs}} f_{rs,k,t}^{ch} = \gamma_1 \gamma_2 D_{rs,t}^{UTN} : \pi_{rs,t}^{ch}, \forall rs, \forall t \quad (C7)$$

$$\sum_{k \in K_{rs}} f_{rs,k,t}^{non} = (1 - \gamma_1 \gamma_2) D_{rs,t}^{UTN} : \pi_{rs,t}^{non}, \forall rs, \forall t \quad (C8)$$

$$f_{rs,k,t}^{ch} \geq 0, f_{rs,k,t}^{non} \geq 0, \forall k \in K_{rs}, (r, s) \in OD, \forall t \quad (C9)$$

$$x_{a,t}^{ch} = \sum_{rs} \sum_k \Lambda_{a,k}^{rs} \cdot f_{rs,k,t}^{ch} : \mu_{a,t}^{ch}, \forall rs, k, a, t \quad (C10)$$

$$x_{a,t}^{non} = \sum_{rs} \sum_k \Lambda_{a,k}^{rs} \cdot f_{rs,k,t}^{non} : \mu_{a,t}^{non}, \forall rs, k, a, t \quad (C11)$$

$$\lambda_{a,t} \geq 0, \forall a, \forall t \quad (C12)$$

$$\pi_{rs,t}^{ch} - \sum_a ([\Lambda_{a,k}^{rs}]^T \cdot \mu_{a,t}^{ch}) \leq 0, \forall rs, \forall t \quad (C13)$$

$$\pi_{rs,t}^{non} - \sum_a ([\Lambda_{a,k}^{rs}]^T \cdot \mu_{a,t}^{non}) \leq 0, \forall rs, \forall t \quad (C14)$$

$$\mu_{a,t}^{ch} - \lambda_{a,t} = t_a^0, \forall a \in T_A \quad (C15)$$

$$\mu_{a,t}^{non} - \lambda_{a,t} = t_a^0, \forall a \in T_A \quad (C16)$$

$$\begin{aligned} & \gamma_1 \gamma_2 \sum_t \sum_{rs} \pi_{rs,t}^{ch} D_{rs,t}^{UTN} + (1 - \gamma_1 \gamma_2) \sum_t \sum_{rs} \pi_{rs,t}^{non} D_{rs,t}^{UTN} \\ &= \sum_t \sum_a [t_a^0 (x_{a,t}^{ch} + x_{a,t}^{non}) + c_a \lambda_{a,t}] \end{aligned} \quad (C17)$$

$$\sum_h f_{h,t}^{assi} = \gamma_1 \gamma_2 \sum_{rs} D_{rs,t}^{UTN}, \forall t \quad (C18)$$

$$0 \leq f_{h,t}^{assi} \leq N_h^{port}, \forall h \in \Omega \quad (C19)$$

$$f_{h,t}^{assi} \leq \sum_{rs} \sum_k (X_{k,h}^{rs} \cdot f_{rs,k,t}^{ch}), \forall h, \forall t \quad (C20)$$

$$f_{rs,k,t}^{ch} \leq \sum_h ([X_{k,h}^{rs}]^T \cdot f_{h,t}^{assi}), \forall rs, k, t \quad (C21)$$

$$P_{h,t}^{ev} = \Delta p_{h,t} \cdot f_{h,t}^{assi}, \forall h \in \Omega \quad (C22)$$

The road traffic flow constraints are imposed in (C5-6), where $x_{a,t}$ and c_a are the traffic flow and road capacity of road a , respectively. The relationship of the path flow and traffic demand is indicated in (C7-9), where $f_{rs,k,t}^{ch}$ and $f_{rs,k,t}^{non}$ are the path flow of charging and non-charging vehicles on path k of O-D pair rs . γ_1 is the percentage of EVs with respect to all vehicles, and γ_2 is the proportion of charging EVs with respect to all EVs. $D_{rs,t}^{UTN}$ is the traffic demand of O-D pair rs . (C10-11) impose the relation of road flow and path flow, where $\Lambda = \{\Lambda_{a,k}^{rs}, \forall rs, a, k\}$ is the corresponding road-path correlation matrix. Eq. (C12-17) constrain the dual variables of original constraints, where $\pi_{rs,t}^{ch}$, $\pi_{rs,t}^{non}$, $\mu_{a,t}^{ch}$ and $\mu_{a,t}^{non}$ are the dual variables of (C7-8) and (C10-11), respectively. $[\cdot]^T$ means matrix transposition. Eq. (C17) shows the strong dual condition, which guarantees the same solution for the original and dual problems. Eq. (C18) means all the charging EVs are assigned to EVCSs, where $f_{h,t}^{assi}$ is the assigned EV flows to EVCS h . The assigned EV flows cannot exceed the EV ports of EVCSs as illustrated in (C19). Eq. (C20-21) relate the EV flows assigned to an EVCS and traffic flow through the corresponding road, where the correlation matrix $X = \{X_{k,h}^{rs}, \forall rs, k, h\}$ relates the EVCS location to the travel path. The charging load assignment for an EVCS is proportional to assigned EV flows, as shown in (C22).

Thus, the EV charging load assignment problem in UTN is formulated as

$$\begin{aligned} & \text{minimize } F_{UTN}^{TSO}(\mathbf{x}^{UTN}, \mathbf{x}^{dual}, \mathbf{f}^{CS}, \mathbf{P}^{EV}) \\ & \text{s.t. (C2)-(C22)} \end{aligned} \quad (C23)$$

where \mathbf{x}^{UTN} denotes the UTN decision variable vector; \mathbf{x}^{dual} means the dual variable vector in TAP; \mathbf{f}^{CS} and \mathbf{P}^{EV} indicate the EV allocation variable vectors regarding traffic flow and charging load.

APPENDIX D: DETAILED OPERATION CONSTRAINTS FOR DGs AND BESSs

• Constraints of DGs

$$P_i^{dg, \min} + R_i^{dn} \leq P_{i,t}^{dg} \leq P_i^{dg, \max} - R_i^{up}, \forall i \in I_g, t \quad (D1)$$

$$-RD_i \Delta t \leq P_{i,t}^{dg} - P_{i,t-1}^{dg} \leq RU_i \Delta t, \forall i \in I_g, t \quad (D2)$$

$$0 \leq R_{i,t}^{up} \leq RU_i \Delta t, 0 \leq R_{i,t}^{dn} \leq RD_i \Delta t, \forall i \in I_g, t \quad (D3)$$

$$P_{i,t}^{dg} \cdot \theta_i^{\min} \leq Q_{i,t}^{dg} \leq P_{i,t}^{dg} \cdot \theta_i^{\max}, \forall i \in I_g, t \quad (D4)$$

$$P_{i,t}^{dg} = \sum_{\phi} P_{i,\phi,t}^{dg}, Q_{i,t}^{dg} = \sum_{\phi} Q_{i,\phi,t}^{dg}, \forall i, t \quad (D5)$$

Eq. (D1) constrains the power output of DGs, where $P_i^{dg, \max}$, $P_i^{dg, \min}$ indicate the maximum and minimum power output; $R_{i,t}^{up}$, $R_{i,t}^{dn}$ are the up/down reserve provided by DG i . The ramping limitation of DGs is illustrated in (D2). The provided reserve cannot exceed the ramping limitation as shown in (D3). The reactive power of DGs is limited by (D4), where θ_i^{\max} and

θ_i^{\min} are the maximum and minimum power factors. The three-phase active and reactive power of DGs are expressed in (D5).

♦ Constraints of grid BESSs

$$E_{i,t}^{\text{ess}} = E_{i,t-1}^{\text{ess}} + (P_{i,t}^{\text{ch}} \eta_i^{\text{ch}} - P_{i,t}^{\text{dis}} / \eta_i^{\text{dis}}) \Delta t, \forall i \in I_s, t \quad (\text{D6})$$

$$E_{i,t}^{\text{ess},\min} \leq E_{i,t}^{\text{ess}} \leq E_{i,t}^{\text{ess},\max}, \forall i \in I_s, t \quad (\text{D7})$$

$$0 \leq P_{i,t}^{\text{ch}} + R_{i,t}^{\text{dn}} \leq P_{i,t}^{\text{ch},\max}, \forall i \in I_s, t \quad (\text{D8})$$

$$0 \leq P_{i,t}^{\text{dis}} + R_{i,t}^{\text{up}} \leq P_{i,t}^{\text{dis},\max}, \forall i \in I_s, t \quad (\text{D9})$$

$$-\alpha_i^{\max} |P_{i,t}^{\text{ch}} - P_{i,t}^{\text{dis}}| \leq Q_{i,t}^{\text{ess}} \leq \alpha_i^{\max} |P_{i,t}^{\text{ch}} - P_{i,t}^{\text{dis}}|, \forall i \in I_s, t \quad (\text{D10})$$

$$P_{i,t}^{\text{ch}} = \sum_{\phi} P_{i,\phi,t}^{\text{ch}}, P_{i,t}^{\text{dis}} = \sum_{\phi} P_{i,\phi,t}^{\text{dis}}, \forall i \in I_s, t \quad (\text{D11})$$

$$Q_{i,t}^{\text{ess}} = \sum_{\phi} Q_{i,\phi,t}^{\text{ess}}, \forall i \in I_s, t \quad (\text{D12})$$

Eq. (D6-7) indicates the charging state of grid BESSs, where η_i^{ch} and η_i^{dis} are the charging & discharging efficiency; $E_{i,t}^{\text{ess},\max}$ and $E_{i,t}^{\text{ess},\min}$ are the maximum & minimum energy storage of grid BESSs. The reserve provided by grid BESSs is constrained by (D8-9), where $P_{i,t}^{\text{ch},\max}$ and $P_{i,t}^{\text{dis},\max}$ means the maximum charging & discharging power. Eq. (D10) limits the reactive power from grid BESSs, where α_i^{\max} is the maximum power factor. Eq. (D11-12) express the three-phase active and reactive power.

APPENDIX E: PROOF FOR PROPOSITION 1

Here, we derive the sensitivity matrixes of system variables (i.e., line flow and nodal voltage) respond to nodal power, which express the influences of nodal power on line flow and nodal voltage. Inspired by *power transmission distribution factors* (PTDF), we introduce sensitivity matrix $\mathbf{A} \in \mathbb{R}^{3L \times 3N}$, where L is the number of lines and N is the number of nodes, to map the change of nodal power at each node to the change of line power flow in three-phase system. Note that the PDN system in this paper is radial, thus, the \mathbf{A} can be constructed as:

$$a_{l,i}^{\phi,\phi'} := \begin{cases} 1 & \text{if line } l \text{ of phase } \phi \text{ is the part of the} \\ & \text{path from root to bus } i \text{ at phase } \phi', \forall l, i, \phi, \phi' \quad (\text{E1}) \\ 0 & \text{otherwise} \end{cases}$$

where $a_{l,i}^{\phi,\phi'}$ indicates the element in column $3(i-1) + \phi'$ of row $3(l-1) + \phi$ of the matrix \mathbf{A} . Thus, the change of nodal power to the change of each line power flow in three-phase system can be described as:

$$\Delta \mathbf{P}_{\text{line}} = \mathbf{A} \cdot \Delta \mathbf{P}, \forall l, \phi \quad (\text{E2})$$

$$\Delta \mathbf{P}_{\text{line}} = [\Delta P_1^a; \Delta P_1^b; \Delta P_1^c; \dots; \Delta P_L^a; \Delta P_L^b; \Delta P_L^c] \in \mathbb{R}^{3L \times 1} \quad (\text{E3})$$

$$\Delta \mathbf{P} = [\Delta P_1^a; \Delta P_1^b; \Delta P_1^c; \dots; \Delta P_N^a; \Delta P_N^b; \Delta P_N^c] \in \mathbb{R}^{3N \times 1} \quad (\text{E4})$$

where $\Delta \mathbf{P}^l$ indicates the change vector of active line flow and ΔP_l^{ϕ} means the active flow change of line l at phase ϕ ; $\Delta \mathbf{P}$ indicates the change vector of nodal power and ΔP_i^{ϕ} means the nodal power change of node i at phase ϕ . Thus, for specific line l 's active power change at phase ϕ can be calculated as:

$$\Delta P_l^{\phi} = \mathbf{A}_{l,*}^{\phi} \Delta \mathbf{P}, \forall l, \phi \quad (\text{E5})$$

where $\mathbf{A}_{l,*}^{\phi} \in \mathbb{R}^{1 \times 3N}$ means the whole row $3(l-1) + \phi$ of sensitivity matrix \mathbf{A} . Similarly, the reactive line flow change and the reactive nodal power change should satisfy:

$$\Delta Q_l^{\phi} = \mathbf{A}_{l,*}^{\phi} \Delta \mathbf{Q}, \forall l, \phi \quad (\text{E6})$$

Thus, the sensitivity matrixes of line flow and voltage to nodal power can be described as:

$$\mathbf{JP}_{l,t}^{\phi} = \frac{\partial P_{l,t}^{\phi}}{\partial \mathbf{S}_i} = \left[\frac{\partial P_{l,t}^{\phi}}{\partial P_t}, \frac{\partial P_{l,t}^{\phi}}{\partial Q_t} \right] = [\mathbf{A}_{l,*}^{\phi}, \mathbf{0}^{1 \times 3N}] \in \mathbb{R}^{1 \times 6N} \quad (\text{E7})$$

$$\mathbf{JQ}_{l,t}^{\phi} = \frac{\partial Q_{l,t}^{\phi}}{\partial \mathbf{S}_i} = \left[\frac{\partial Q_{l,t}^{\phi}}{\partial P_t}, \frac{\partial Q_{l,t}^{\phi}}{\partial Q_t} \right] = [\mathbf{0}^{1 \times 3N}, \mathbf{A}_{l,*}^{\phi}] \in \mathbb{R}^{1 \times 6N} \quad (\text{E8})$$

where $\mathbf{JP}_{l,t}^{\phi}$ and $\mathbf{JQ}_{l,t}^{\phi}$ indicate the sensitivity matrixes of active and reactive line flow (line l at phase ϕ) to nodal power. Collecting the sensitivity matrixes of individual lines, the following coefficient matrixes can be formulated as:

$$\mathbf{JP} = [\mathbf{JP}_1^a; \mathbf{JP}_1^b; \mathbf{JP}_1^c; \dots; \mathbf{JP}_L^a; \mathbf{JP}_L^b; \mathbf{JP}_L^c] \in \mathbb{R}^{3L \times 6N} \quad (\text{E9})$$

$$\mathbf{JQ} = [\mathbf{JQ}_1^a; \mathbf{JQ}_1^b; \mathbf{JQ}_1^c; \dots; \mathbf{JQ}_L^a; \mathbf{JQ}_L^b; \mathbf{JQ}_L^c] \in \mathbb{R}^{3L \times 6N} \quad (\text{E10})$$

The original voltage drop of line l at phase ϕ can be expressed as:

$$u_i^{\phi} - u_j^{\phi} = 2(\hat{\mathbf{R}}_l \cdot \mathbf{P}_l + \hat{\mathbf{X}}_l \cdot \mathbf{Q}_l), i = o(l), j = r(l) \quad (\text{E11})$$

where $\hat{\mathbf{R}}_l$ and $\hat{\mathbf{X}}_l$ are the real part and the imaginary part of the transformed sequence impedance matrix $\hat{\mathbf{Z}}_l$ of line l . We can find that the voltage drop of line sides is just related to the line flow. Since the root voltage, i.e., substation voltage, is always fixed as the reference voltage. Thus, a certain nodal voltage change such as node i is related to all the line flow changes of the path from root to node i . Thus, the nodal voltage change of node i at phase ϕ can be calculated as:

$$\Delta u_i^{\phi} = -2 \cdot [\mathbf{A}_{*i}^{\phi}]^T \cdot (\hat{\mathbf{R}} \cdot \Delta \mathbf{P}_{\text{line}} + \hat{\mathbf{X}} \cdot \Delta \mathbf{Q}_{\text{line}}) \quad (\text{E12})$$

$$\hat{\mathbf{R}} = \text{diag}\{\hat{\mathbf{R}}_1, \dots, \hat{\mathbf{R}}_L\} \in \mathbb{R}^{3L \times 3L} \quad (\text{E13})$$

$$\hat{\mathbf{X}} = \text{diag}\{\hat{\mathbf{X}}_1, \dots, \hat{\mathbf{X}}_L\} \in \mathbb{R}^{3L \times 3L} \quad (\text{E14})$$

where \mathbf{A}_{*i}^{ϕ} indicates the column $3(i-1) + \phi$ of matrix \mathbf{A} ; $\hat{\mathbf{R}}$ and $\hat{\mathbf{X}}$ are the matrixes constructed from the transformed sequence impedance matrix of each line as shown in (E13) and (E14). Thus, the sensitivity matrix of nodal voltage (node i at phase ϕ) to nodal power can be derived as:

$$\mathbf{JV}_{i,t}^{\phi} = \frac{\partial u_{i,t}^{\phi}}{\partial \mathbf{S}_i} = -2[\mathbf{A}_{*i}^{\phi}]^T \cdot [\hat{\mathbf{R}} \cdot \mathbf{JP} + \hat{\mathbf{X}} \cdot \mathbf{JQ}] \in \mathbb{R}^{1 \times 6N} \quad (\text{E15})$$

Collecting the sensitivity matrixes of individual nodal voltage, the following coefficient matrixes can be formulated as:

$$\mathbf{JV} = [\mathbf{JV}_1^a; \mathbf{JV}_1^b; \mathbf{JV}_1^c; \dots; \mathbf{JV}_N^a; \mathbf{JV}_N^b; \mathbf{JV}_N^c] \quad (\text{E16})$$

APPENDIX F: PROOF FOR PROPOSITION 2

Through proposed affine policy and balance participation factor, the change of nodal power to the change of uncertain net electric load can be depicted in (16). After the sensitivity matrix analysis of whole system, the change of line flow and nodal voltage to the change of nodal power can be described in (19). Thus, the change of line flow and nodal voltage to the change

of uncertain net electric load can be derived as below after substituting (16) into (19):

$$\Delta P_l^\phi = \mathbf{J}P_{l,t}^\phi \Delta S = \mathbf{J}P_{l,t}^\phi \begin{bmatrix} \Delta P \\ \Delta Q \end{bmatrix} = \mathbf{J}P_{l,t}^\phi \begin{bmatrix} \mathbf{D} - \mathbf{B} \\ \alpha \odot \mathbf{D} - \alpha \odot \mathbf{B} \end{bmatrix} \xi \quad (\text{F1})$$

$$= \mathbf{X}P_{l,t}^\phi \xi, \forall l, \phi$$

$$\text{where } \mathbf{X}P_{l,t}^\phi = \mathbf{J}P_{l,t}^\phi \cdot \begin{bmatrix} \mathbf{D} - \mathbf{B} \\ \alpha \odot \mathbf{D} - \alpha \odot \mathbf{B} \end{bmatrix}, \forall l, \phi, t \quad (\text{F2})$$

where α the given power factor vector. Thus, the responding functions of active line flow to nodal net electric load deviation ξ can be written as:

$$\tilde{P}_{l,t}^\phi = P_{l,t}^\phi + \mathbf{X}P_{l,t}^\phi \cdot \xi_t, \forall l, \phi, t \quad (\text{F3})$$

Similarly, the responding functions of reactive line flow and nodal voltage to nodal net electric load deviation ξ can be written as:

$$\tilde{Q}_{l,t}^\phi = Q_{l,t}^\phi + \mathbf{X}Q_{l,t}^\phi \cdot \xi_t, \forall l, \phi, t \quad (\text{F4})$$

$$\text{where } \mathbf{X}Q_{l,t}^\phi = \mathbf{J}Q_{l,t}^\phi \cdot \begin{bmatrix} \mathbf{D} - \mathbf{B} \\ \alpha \odot \mathbf{D} - \alpha \odot \mathbf{B} \end{bmatrix}, \forall l, \phi, t \quad (\text{F5})$$

$$\tilde{u}_{i,t}^\phi = u_{i,t}^\phi + \mathbf{X}V_{i,t}^\phi \cdot \xi_t, \forall i, \phi, t \quad (\text{F6})$$

$$\text{where } \mathbf{X}V_{i,t}^\phi = \mathbf{J}V_{i,t}^\phi \cdot \begin{bmatrix} \mathbf{D} - \mathbf{B} \\ \alpha \odot \mathbf{D} - \alpha \odot \mathbf{B} \end{bmatrix}, \forall i, \phi, t \quad (\text{F7})$$

APPENDIX G: ADDITIONAL REFERENCES

- [G1] W. Gan et al., "Coordinated Planning of Transportation and Electric Power Networks With the Proliferation of Electric Vehicles," *IEEE Trans. on Smart Grid*, vol. 11, no. 5, pp. 4005–4016, Sep. 2020.
- [G2] L. Affolabi, M. Shahidehpour, F. Rahimi, F. Aminifar, K. Nodehi, and S. Mokhtari, "DSO market for transactive scheduling of electric vehicle charging stations in constrained hierarchical power distribution and urban transportation networks," *IEEE Trans. Transp. Electr.*, pp. 1-1, 2023.
- [G3] S. Peng, X. Lin, J. Tang, K. Xie, F. Ponci, A. Monti, and W. Li, "Probabilistic power flow of AC/DC hybrid grids with addressing boundary issue of correlated uncertainty sources," *IEEE Trans. Sustainable Energy*, vol. 13, no. 3, pp. 1607-1619, 2022.
- [G4] S. Peng, J. Tang, and W. Li, "Probabilistic power flow for AC/vsc-mtcd hybrid grids considering rank correlation among diverse uncertainty sources," *IEEE Trans. Power Syst.*, vol. 32, no. 5, pp. 4035-4044, 2017.
- [G5] X. Wu, H. Li, X. Wang, and W. Zhao, "Cooperative operation for wind turbines and hydrogen fueling stations with on-site hydrogen production," *IEEE Trans. Sustainable Energy*, vol. 11, no. 4, pp. 2775-2789, 2020.
- [G6] H. Wang, Z. Bie, and H. Ye, "Locational marginal pricing for flexibility and uncertainty with moment information," *IEEE Trans. Power Syst.*, vol. 38, no. 3, pp. 2761-2775, 2023.